Separation and Purification Technology 376 (2025) 134064

Contents lists available at ScienceDirect

Separation and Purification Technology

journal homepage: www.elsevier.com/locate/seppur

A road map to planar asymmetric oxygen transport ceramic membranes: An example case based on Fe-doped $SrTiO_3$

Fanlin Zeng [a,*], Wendelin Deibert [a], Kai Wilkner [a], Wilhelm Albert Meulenberg [a,b], Stefan Baumann [a]

[a] Forschungszentrum Jülich GmbH, Institute of Energy Materials and Devices, 52425 Jülich, Germany
[b] University of Twente, Faculty of Science and Technology, Inorganic Membranes, P.O. Box 217, 7500 AE Enschede, the Netherlands

ARTICLE INFO

Editor: Gaohong He

Keywords:
Asymmetric ceramic membranes
Scalable fabrication
Sequential tape casting
Porous support layer
Oxygen permeation
Sintering optimization

ABSTRACT

Scalable fabrication of asymmetric oxygen transport membranes offers great potential for oxygen production, energy conversion and chemical synthesis. This study develops a sequential tape casting process utilizing commercially sourced ceramic powders to fabricate planar asymmetric membranes. By systematically adjusting key parameters – particle size, pore former type, casting blade gaps, and sintering conditions, the process achieves bilayer membranes with enhanced compatibility, mechanical integrity, and oxygen transport efficiency. Controlled ball milling yields appropriate average particle sizes (≥0.6 μm) and specific surface areas (≤5 m^2/g), preventing cracking and improving homogeneity of ceramic tapes. Through the use of calibrated blade gaps, a corn starch pore former, and sintering at 1350 °C, a bilayer membrane configuration is obtained with distinct porous and dense layers. Large membranes up to ~87 mm in diameters are further shielded from crack formation by a cautious heating ramp (0.5 K/min) during debinding between 200 °C and 900 °C. High oxygen permeation rates are demonstrated for the asymmetric membranes because of the optimized bilayer configuration, which includes a support layer with a high porosity, a large surface area, and rapid gas diffusion pathways. Additionally, the negative effects from secondary phase formation are eliminated by reducing the sintering time to four hours. Surface activation coatings further improve performance, particularly at low temperatures (650 °C–750 °C) with $La_{0.58}Sr_{0.4}Co_{0.2}Fe_{0.8}O_{3-\delta}$ (LSCF) coating of superior surface exchange kinetics. This work is a significant step towards industrial applications by establishing an exemplified framework for producing and applying high-performance, scalable oxygen transport membranes.

1. Introduction

Oxygen transport membranes, fabricated from oxide ceramics with 100 % selectivity toward oxygen [1], serve as key components within membrane reactors – an electrochemical technology that holds significant promise for applications such as energy-efficient oxygen production [2], and oxyfuel combustion [3,4], as well as partial oxidation of hydrocarbons [5–8], yielding high-value products like syngas and hydrogen. The membrane reactor operates at high temperatures (preferably in the range of 800 °C–1000 °C) and is driven by an oxygen partial pressure gradient across the membrane, requiring no input of external electrical potential.

When integrated with solar thermal energy as the heat source, this system facilitates green hydrogen production. As illustrated in Fig. 1, steam (H_2O) and methane (CH_4) are introduced on opposite sides of the membrane. Continuous steam thermolysis on one side generates hydrogen (H_2), while oxygen (O_2), as a by-product, permeates through the membrane to the opposing side, where it drives the partial oxidation of methane into syngas [7]. Necessary catalysts, e.g., M/$Ce_{0.85}Sm_{0.15}O_{1.925}$ (M = Ru, Pd and Pt) [9], are applied at the two sides to support the individual reactions. The efficient separation and in-situ transport of oxygen across the membrane enhances both the thermodynamics and kinetics of the overall process, making the membrane reactor a versatile and sustainable solution for the production of energy carriers and chemicals.

Doped alkaline earth titanates, such as $SrTiO_3$ doped by Mg or Fe (≤25 mol%) at the Ti site, are among the most promising membrane materials due to their exceptional chemical stability and relatively low chemical expansion in reducing environments [10,11], a key advantage over classic perovskite-type oxides like barium/lanthanum strontium

* Corresponding author.
E-mail address: f.zeng@fz-juelich.de (F. Zeng).

https://doi.org/10.1016/j.seppur.2025.134064
Received 14 March 2025; Received in revised form 13 June 2025; Accepted 19 June 2025
Available online 20 June 2025

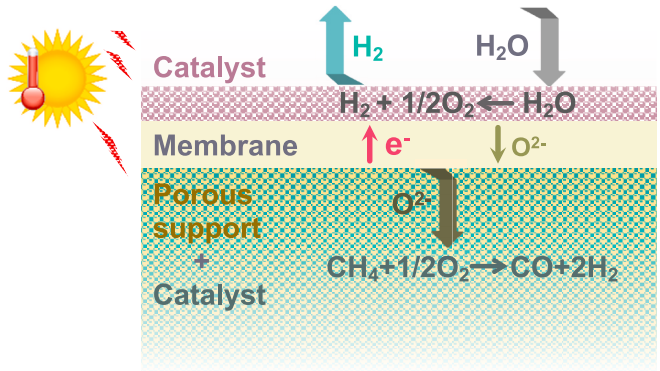

Fig. 1. Working principle of a solar thermal driven membrane reactor.

cobalt ferrite. However, a significant limitation arises at intermediate oxygen partial pressures (~10^{-8}–10^{-6} bar) [12–14], where a conductivity minimum occurs due to the depletion of charge carriers. The performance of doped $SrTiO_3$ can be hindered in applications, such as water splitting, involving operation conditions at intermediate oxygen partial pressures.

To counterbalance the conductivity limitation, a widely adopted strategy is to reduce the membrane thickness, effectively shortening the transport pathways and enhancing permeation efficiency [15,16]. Whereas, when a free-standing membrane approaches a thickness of ca. 100 μm, its mechanical integrity becomes compromised, making it prone to fragility during production, handling, and operation. To address this, an asymmetric membrane structure has been developed, where a dense thin membrane layer is supported by a thicker, porous substrate, as depicted in Fig. 1. This design provides the necessary mechanical support while maintaining the membrane's functional properties. Nonetheless, the porous support layer introduces gas diffusion resistance, which can negatively impact overall performance [15]. This resistance can be minimized by optimizing the porosity of the support layer [17] or by designing straight pore channels to facilitate more efficient gas transport [18,19].

Up to date, a variety of powder-based manufacturing techniques have been extensively explored for fabricating asymmetric membranes. For instances, asymmetric $Ba_{0.5}Sr_{0.5}Co_{0.8}Fe_{0.2}O_{3-\delta}$ [20], $La_{5.5}W_{0.6}Mo_{0.4}O_{11.25-\delta}F_{0.05}$ [21] and $BaCe_{0.85}Tb_{0.05}Zr_{0.1}O_{3-\delta}$ [22] membranes have sintered from co-pressed compacts of support and membrane powders. Q. Li et al. demonstrated the fabrication of asymmetric $Ce_{0.85}Sm_{0.15}O_{1.925}$-$Sm_{0.6}Sr_{0.4}FeO_{3-\delta}$ composite membranes through the convenient method of acid leaching one side of sintered single-layer membranes [23]. X. Meng et al. successfully obtained asymmetric $BaCo_{0.7}Fe_{0.2}Nb_{0.1}O_{3-\delta}$ membranes by dip-coating a membrane slurry onto porous substrates, followed by co-sintering [24]. Other techniques, such as slip casting and screen printing, have also been employed to coat $La_{1-x}Sr_xCo_{1-y}Fe_yO_{3-\delta}$ membrane layer onto various porous substrates [25].

Among these methods, tape casting has emerged as one of the most dominant techniques for fabricating asymmetric membranes. This method allows either for the independent casting of the membrane and support layers, where after these layers are subsequently stacked, laminated, and co-sintered [26–29], or for the sequential casting of the membrane and support layers in a continuous process followed by co-sintering [15,30–35]. The sequential tape casting approach, being theoretically more efficient and streamlined, have been widely and successfully utilized to produce small-sized membrane components [15,30–32]. This approach is in fact particularly promising for large-sized membrane production [33,36], which is critical for increasing membrane surface area and enhancing permeation efficiency. However, the literature reveals a persistent gap in documenting the technical and practical challenges associated with scaling up this method. The transition from small-scale laboratory prototypes to industrial-scale membrane manufacturing remains inadequately explored. The difficulties in scaling are linked to the complexities of controlling defect formation, optimizing layer adhesion, and ensuring the mechanical integrity of the membrane during both casting and co-sintering phases to achieve large-sized membranes with high flatness and gas tightness. These unresolved technical barriers hinder the broader adoption of sequential tape casting in industrial applications, calling for more focused research and deeper exploration to systematically address the engineering challenges of large-scale production and unlock the method's full potential.

In this work, we undertake a comprehensive exploration of a technological methodology for the fabrication of planar asymmetric oxygen transport ceramic membranes with various sizes, exemplified by the use of Fe-doped $SrTiO_3$ as a representative material. Our approach employs sequential tape casting, initiated from commercially available precursor powders. The research framework is multifaceted, addressing both the intricate aspects of process optimization and the underlying physicochemical mechanisms governing membrane performance.

2. Experimental

2.1. Tape casting of single-layer and asymmetric membranes

A technologic routine for fabrication of asymmetric membranes is illustrated in Fig. S1. The processes were initiated from ceramic powders with a specific composition of $Sr_{0.98}Ti_{0.75}Fe_{0.25}O_{3-\delta}$ (S98TF25), which were purchased in a 10 kg batch from WZR ceramic solutions GmbH, Rheinbach, Germany. The small amount of strontium deficiency (2 mol. %) was introduced to enhance the sinterability [37]. The overall processes involved in the current study are broken down into four steps, as elaborated below.

2.1.1. Powder particle size optimization via ball milling

The ball milling procedures were conducted on a roller bench. The ceramic powder, ZrO_2 balls (3 mm in diameter) and ethanol is mixed according to a weight ratio of 2:3:2. They are filled in polyethylene bottle with a volume of 0.5 L (ca. 76 mm in diameter) and 2 L (ca. 119 mm in diameter) up to ca. 69 % and ca. 28 % of the total volume, respectively. The roller bench is set at a fixed power, which result in rotation speeds of ca. 83 r/min and ca. 54 r/min for 0.5 L and 2 L bottle, respectively. The milling time was varied to be 1 and 3 days for the 0.5 L bottle and controlled to be 3 days for the 2 L bottle.

2.1.2. Slurry preparation

To prepare the slurry for tape casting, the ceramic powders were mixed with solvents (34 wt% ethanol and 66 wt% methylethylketone from AnalytiChem GmbH, Germany), dispersant (Nuosperse FX 9086 from Elementis Inc., UK), binder (polyvinyl butyral 98 from Solutia Inc., USA), plasticizers (equal amount of OXSOFT 3G8 from OXEA GmbH, Germany and Polyethylene glycol 400 from Merk KGaA, Germany), and pore former (either corn starch from Cargill Deutschland GmbH, Germany or rice starch from BENEO-Remy N.V., Belgium), according to the weight ratios given in Fig. S2. The additives were added sequentially in 3 steps into the ceramic powders within polyethylene bottles. Solvents and dispersant were first added, then the pore former (only for the support layer slurry) was added, and at last, the rest of the additives were added. After each step, the slurry was homogenized by a planetary centrifugal vacuum mixer (ARV-310 from THINKY CORPORATION, Tokyo, Japan) at 1300 r/min for 5 mins with the addition of ZrO_2 milling balls having a diameter of 3 mm and a weight equal to the one of the ceramic powders. After homogenization, the hot slurry must be cooled down to room temperature before the next step. The slurry was kept stationary and saturated for ~72 h, and homogenized again prior to tape casting.

2.1.3. Tape casting

The tape casting was performed at room temperature and atmospheric humidity using a micro-tape casting device (KAROcast 300-7 from KMS Automation GmbH, Germany). A casting speed of 2.5 mm/s or 5 mm/s was applied. The blade gaps during slurry casting were modified to adjust the layer thickness of the tape. For one-layer tape casting, the membrane and support slurry were cast at blade gaps of 0.9 mm and 1 mm, respectively. For the bilayer tape casting, the membrane slurry was first cast at blade gaps of 0.1 mm or 0.2 mm, followed by the casting of the support slurry on top of the dried membrane tape at blade gaps of 1 mm or 0.75 mm. The drying time of each tape was ensured to be no shorter than four hours. Table 1 summarizes the ball milling and tape casting parameters applied for different types of bilayer tapes.

2.1.4. Shaping, sintering and flattening

Membrane disks with diameters ranging from 20 mm to 110 mm were punched or cut out of the dried tapes, and sintered by different programs, where the temperature varied between 1300 °C and 1400 °C at a heating/cooling rate of 5 K/min. A specific low heating rate of 0.5 K/min will also be applied. The warped membranes were flattened by laying ZrO_2 plate(s) on top at annealing temperatures of 100 °C below sintering temperature, i.e., 1200 °C or 1300 °C. The load was controlled, by the weight of ZrO_2 plate, to be varied among nominal values of 0.1 g/mm^2, 0.2 g/mm^2, and 0.3 g/mm^2, which is calculated assuming the load is homogeneously distributed on the entire membrane surface.

The warpage and shrinkage behavior of the sample during thermal treatment were continuously recorded using an optical dilatometer (TOMMI plus, Fraunhofer ISC Würzburg, Germany), which consists of a furnace with quartz glass windows, a light source, and a camera.

The sample topography was investigated using an optical profilometer (Cyber Scan CT350T, cyberTECHNOLOGIES GmbH, Germany) equipped with a CHR3000 sensor head, which has a resolution of 0.1 µm and works on the principle of chromatic aberration. The measurements in this work were performed with an x and y step width of 0.5 mm.

2.2. Powder and membrane characterization

2.2.1. Powder particle size

The powder particle size distribution was determined by the laser diffraction method based on Mie theory using a Horiba LA 950 V2 analyzer (Retsch Technology GmbH, Haan, Germany). The powder specific surface area was measured by the Brunauer-Emmett-Teller (BET) single-point method by low-temperature N_2 adsorption using Areameter II (Ströhlein Instruments, Viersen, Germany).

2.2.2. Crystalline structure and microstructure

Crystalline structure and phase compositions were tested by X-ray diffraction (XRD) using a Bruker D4 ENDEAVOR diffractometer at room temperature with Cu Kα radiation in the 2θ range from 10° to 80°. The XRD patterns were analyzed using TOPAS software with crystal structure data from the Inorganic Crystal Structure Database (ICSD) (FIZ Karlsruhe GmbH) as references.

Microscopic characterization of the microstructures was performed on the polished cross sections of the sintered membranes using scanning electron microscopy (Merlin, Carl Zeiss Microscopy, Oberkochen, Germany), in conjunction with energy-dispersive X-ray spectroscopy (EDS) for elemental analysis. Quantitative porosity evaluation was carried out through digital image analysis utilizing the ImageJ software [38]. To optimize pore segmentation, backscattered electron microscopy (BSEM) images were preferentially selected due to their enhanced contrast relative to the secondary electron microscopy (SEM) images. For each membrane specimen, a minimum of two non-overlapping fields of view, collectively encompassing a surface area over ~0.26 mm^2, were subjected to analysis. Automated thresholding was implemented using the Huang algorithm [39], which yielded the most reliable binarization outcomes. Manual correction was performed on few large pores that were not segmented by the algorithm.

2.2.3. Leakage test

The gas tightness of the sintered membrane was assessed using a Heleak detector (ASM 340, Pfeiffer Vacuum GmbH, Asslar, Germany). Helium was fed at one side of the membrane, while a vacuum was drawn on the other side. The helium flow gas passing through the sample was collected and calculated as helium leakage rate, which should not be above 10^{-4} mbar·L·s^{-1} for a gas-tight membrane.

2.2.4. Performance assessment

Oxygen permeation measurements were conducted using gas-tight bare membranes of varied thicknesses. The membranes exceeding a thickness of approximately 0.3 mm were obtained by sintering of die-pressed powder compacts at 1400 °C for 10 h. While the thin (<223 µm) membranes were produced by tape casting, and sintered at 1350 °C or 1400 °C for 10 h. Necessary grinding and polishing were performed to achieve the targeted thickness, simultaneously removing any surface impurities.

In addition to bare membranes, some membranes were subjected to surface activation to enhance oxygen permeation. This surface activation was achieved through the application of porous coatings on both membrane surfaces, using materials including S98TF25 and $La_{0.58}Sr_{0.4}Co_{0.2}Fe_{0.8}O_{3-\delta}$ (LSCF). The coating process involved a dip-coating technique in which samples were vertically immersed into a ceramic slurry for three times to achieve the desired coating thickness. Each dipping last approximately 5 s, followed by a drying step to ensure proper layer adherence before the next dipping. The ceramic slurries used for dip-coating were prepared by dispersing 10 wt% of ceramic powders in an ethanol solvent, to which 0.1 wt% polyvinyl butyral (PVB) was added as a binder to improve slurry stability and coating uniformity.

Each membrane was integrated into a gas-tight system using a sealing technique that employed gold rings on both sides of the membrane. This assembly was placed in a glass tube and heated to approximately 1020 °C under spring-loaded conditions to ensure a proper seal. Oxygen permeation flux under steady-state conditions was subsequently measured over a temperature range of approximately 1020 °C–850 °C. Air and pure oxygen were used as the feed gases flowing at a rate of 250 ml/min, while argon served as the sweep gas at a rate of 50 ml/min.

Table 1
Summarized ball milling and tape casting parameters.

Bilayer tape	Ball milling of powder		Blade gap (mm)		Casting speed (mm/s)	
	Time (day)	Container size (L)	Membrane Layer	Support layer	Membrane Layer	Support layer
I	–	–	0.1	1	2.5	2.5
II	–	–	0.2	0.75	2.5	2.5
III	1	0.5	0.2	0.75	2.5	2.5
IV	1	0.5	0.2	0.75	2.5	5
V	3	0.5	0.2	0.75	2.5	5
VI	3	2	0.2	0.75	2.5	5

–: Powders are in as-received states without ball milling treatment.

2.2.5. Modelling of membrane performance

The oxygen permeation performance of a membrane is fundamentally determined by its capability to facilitate oxygen transfer across the membrane from the feed gas with high oxygen partial pressure ($p^f_{O_2}$) to the sweep gas with low oxygen partial pressure ($p^s_{O_2}$). This transport process is quantitatively governed by the modified Wagner equation [40–42], as expressed as Eqs. (1)-(3), which accounts for both bulk diffusion and surface exchange kinetics, offering a comprehensive framework to predict and optimize permeation properties.

$$j_{O_2} = \frac{1}{L + 2L_c} \bullet \frac{R \bullet T}{16 \bullet F^2} \bullet \sigma_{amb} \bullet \Delta(\ln p_{O_2}) \tag{1}$$

$$\sigma_{amb} = \frac{\sigma_i \bullet \sigma_e}{\sigma_i + \sigma_e} \tag{2}$$

$$\Delta(\ln p_{O_2}) = \ln \frac{p^f_{O_2}}{p^s_{O_2}} \tag{3}$$

where j_{O_2} denotes the oxygen flux, L is the membrane thickness, T represents the operational temperature, R is the gas constant, and F is the Faraday constant. The parameter σ_{amb} refers to the ambipolar conductivity, incorporating both ionic σ_i and electronic σ_e conductivities within the material. The oxygen partial pressure gradient, $\Delta(\ln p_{O_2})$, serves as the driving force for oxygen permeation across the membrane. An essential concept within this framework is the characteristic thickness L_c, which is the point at which bulk diffusion resistance equals surface exchange resistance [42,43].

The effect of varied driving force can be further normalized using Eq. (4), yielding oxygen permeance (J_{O_2}):

$$J_{O_2} = \frac{j_{O_2}}{\Delta(\ln p_{O_2})} \tag{4}$$

By combining Eqs. (1) and (4), oxygen permeance could be expressed as:

$$J_{O_2} = \frac{1}{L + 2L_c} \bullet \frac{R \bullet T}{16 \bullet F^2} \bullet \sigma_{amb} \tag{5}$$

To account for variations in membrane thickness and ensure comparability of results, the oxygen permeability (P_{O_2}) can be determined. This normalization is achieved using Eq. (6):

$$P_{O_2} = J_{O_2} \bullet (L + 2L_c) \tag{6}$$

The key transport parameters, including σ_{amb} and L_c, are extracted by optimizing their values through a chi-square minimization approach. Specifically, a fit is performed using the chi-square test (Eq. (7)) over a range of parameter values to identify the combination yielding the lowest χ^2, thereby minimizing the deviation from experimentally measured permeability data across samples of varying thicknesses.

$$\chi^2 = \sum_1^n \frac{\left(P^{model}_{O_2,i} - P^{experiment}_{O_2,i}\right)^2}{P^{experiment}_{O_2,i}} \tag{7}$$

3. Results and discussion

3.1. Powder particle size modulation

The ball milling process was performed using a fixed weight ratio of ceramic powders, milling balls, and ethanol (2:3:2), while the operational power of the roller bench remained constant. To modulate the milling effect, variables such as milling time and container size were adjusted.

As presented in Fig. 2, a one-day milling period using a 0.5 L container resulted in a noticeable narrowing of the particle size distribution, accompanied by an increase in specific surface area. Prolonging the milling duration to three days further accentuated the milling effects, leading to additional particle size reduction and a concomitant increase in specific surface area. Conversely, increasing the container size to 2 L, while simultaneously lowering the filling volume from 69 vol % to 28 vol% and decreasing the rotation speed from approximately 83 r/min to 54 r/min, yields a particle size distribution and specific surface area that falls between those achieved by one and three-day milling in the 0.5 L container. This outcome highlights the potential for feasible and precise modulation of particle size and surface area by systematically altering milling parameters, thereby offering enhanced control over downstream processes such as tape casting and sintering.

3.2. Fabrication of individual layers of membrane and support

Before the preparation of the asymmetric membrane, individual layers, comprising both the membrane and its support, were cast as separate tapes from slurries prepared using as-received powders. This casting is performed at a controlled speed of 2.5 mm/s, resulting in flexible tapes that are generally free from cracks and exhibit homogeneous surface characteristics (as shown in Fig. S3). From each tape, at least three disks with initial diameters of ca. 20 mm are punched out for evaluating their in-plane shrinkage (diameter change) and gas-tightness after sintering at various temperatures. This step is critical to assess the thermal compatibility between the membrane and support layers, which in turn enables the sintering profile design required for the asymmetric membrane.

For tapes without any pore former, organic materials burned out during the initial stages of heating, resulting in a temporary decrease in green density and creating voids or pores within the structure. As the temperature rises, these tapes experience a gradual and steady reduction in in-plane dimensions, reaching a plateau after annealing at 1350 °C for 10 h, as revealed in Fig. 3, indicating that the sintering/densification process is complete.

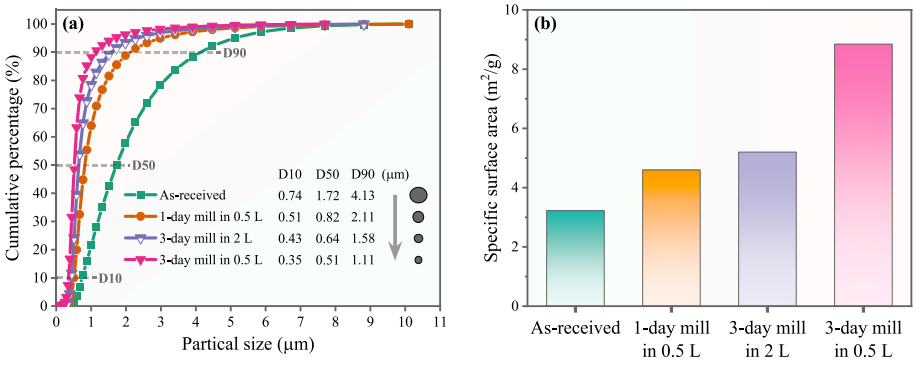

Fig. 2. Particle size distributions (a) and specific surface areas (b) of as-received powders before and after varied ball-milling processes.

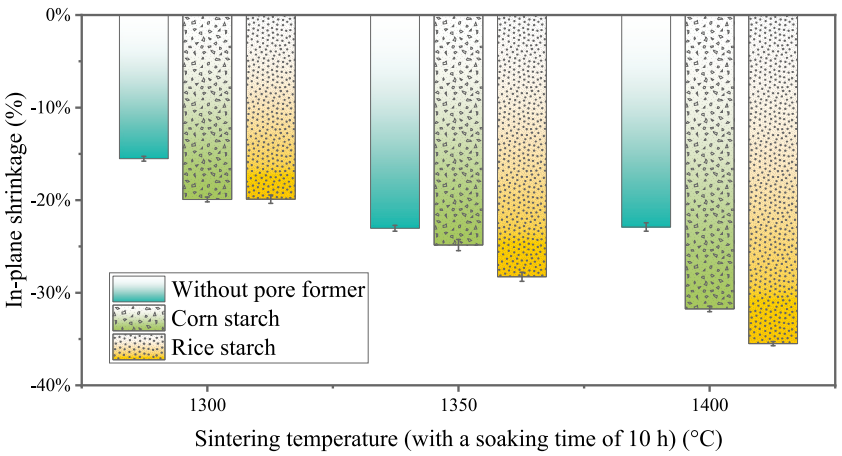

Fig. 3. In-plane shrinkage of individual green tapes prepared using as-received powders, both with and without pore formers (corn or rice starch), as a function of the annealing temperature. (For interpretation of the references to color in this figure legend, the reader is referred to the web version of this article.)

In contrast, tapes that contain pore-forming agents, either corn or rice starch, demonstrate greater shrinkage compared to the membrane tapes after being subjected to individual annealing treatments, as shown in Fig. 3. This disparity is primarily attributed to the decomposition and combustion of starch, in addition to the organic material, below approximately 900 °C, which generates more voids or pores, leading to a greater decrease in green density and, consequently, an increased shrinkage upon subsequent high-temperature annealing. The nature of the pore former also plays a role: corn starch, with its relatively larger particle size compared to rice starch, leads to more significant shrinkage during annealing at temperatures above 1300 °C due to the larger volume of pores generated.

The smallest shrinkage difference, indicative of the highest compatibility, is observed between the membrane tape and the support tape with corn starch as pore former, when an intermediate sintering temperature of 1350 °C is applied.

Moreover, sintering at 1350 °C leads to gas-tight disks from the membrane tape while creates disks with high leakage rates from the support tapes, striking a balance by achieving the desired functional structure for the asymmetric membrane. Whereas, the lowest sintering temperature, i.e., 1300 °C, generally fails to produce gas-tight disks, and the highest temperature, i.e., 1400 °C, results in uniformly gas-tight disks from both membrane and support tapes.

Consequently, for the production of the asymmetric membrane, 1350 °C is selected as the optimal sintering temperature, and corn starch is determined to be the pore-forming agent, ensuring both structural integrity and functional performance.

3.3. Fabrication of asymmetric (bilayer) membranes

3.3.1. Tape morphologies

Bilayer ceramic tapes were fabricated via a sequential tape casting process to produce asymmetric membranes. The same ceramic powders were utilized in both the membrane and support slurries, ensuring material consistency throughout the layers. Each tape's width was maintained at ca. 160 mm.

For slurries containing as-received ceramic powders, two distinct blade gap configurations were employed to control layer thickness, as shown in Table 1 (bilayer tapes I and II), while the casting speed was maintained at 2.5 mm/s. Upon drying, both the membrane and support

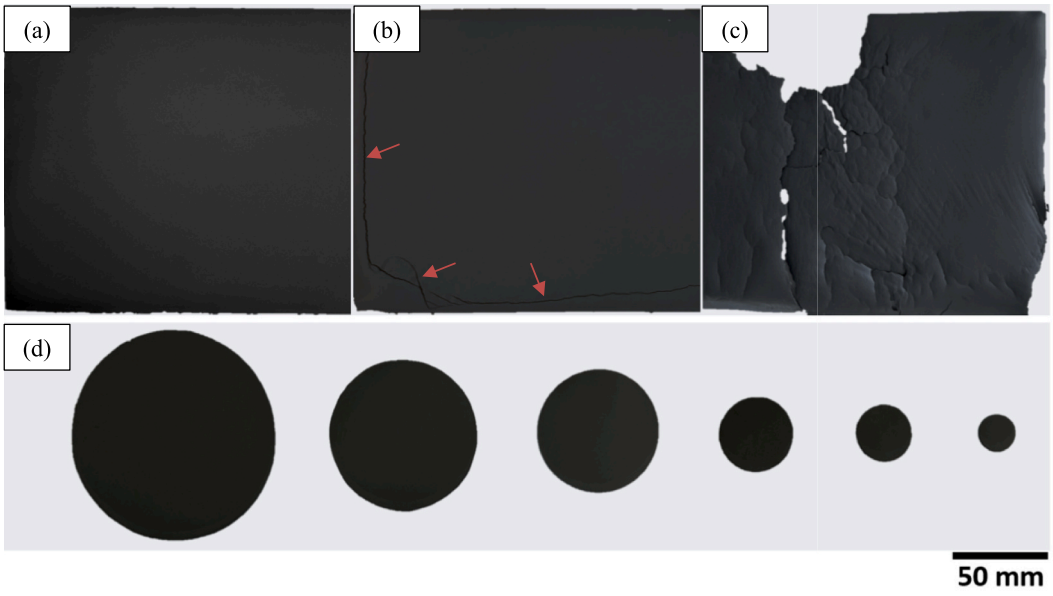

Fig. 4. Optical appearances of bilayer tape II (a), IV (b) and V(c). In (d), disks with diameters ranging from 110 mm to 20 mm, punched from the tapes shown in (a) and (b), are displayed. In (b), the arrows indicate cracks at the edges.

layers exhibited crack-free morphologies, as demonstrated in Fig. 4(a), irrespective of the blade gaps used.

For slurries prepared from ceramic powders that were ball-milled, only one blade gap configuration was applied, as provided in Table 1 (bilayer tapes III, IV, V and VI). After drying, the membrane layers are free of long cracks, although some microcracks were occasionally observed. However, the morphology of the support layer exhibited notable variation depending on the particle size distribution of the ball-milled powders.

When ceramic powders ball-milled for one day in a 0.5 L container were used, the support tapes of the bilayer tape III developed few long cracks and displayed wrinkle-like surface morphologies across plenty of areas (not shown here). Increasing the casting speed to 5 mm/s reduced the wrinkle formations, which were largely confined to the edges of the tapes, although long cracks persisted at the edges (see Fig. 4(b) for bilayer tape IV)). Similar results were observed for bilayer tape VI when using powders ball-milled for three days in a 2 L container.

In contrast, when the smallest particle size powders, obtained after three days of ball milling in a 0.5 L container, were used, the obtained bilayer tape V warps severely and cracked into fragments upon drying, as demonstrated in Fig. 4(c).

The observed variations in tape morphology can be linked to the powder characteristics and casting conditions. The particle size of the ceramic powders plays a crucial role in determining the drying shrinkage and the resulting internal stresses within the tape layers. Larger particles tend to exhibit less shrinkage due to their lower surface area-to-volume ratio, which reduces the capillary forces during solvent evaporation. This explains why tapes casting with as-received powders or powders ball-milled for shorter durations (larger particle sizes) exhibited fewer cracks and generally more stable morphologies.

In contrast, finer particles, especially those produced after extended ball-milling, e.g., three days in a 0.5 L container, pack more densely and are subject to higher capillary pressures during drying. This heightened pressure leads to increased shrinkage, generating higher tensile stresses that exceed the mechanical strength of the green body, thereby causing the severe warping and fragmentation observed (Fig. 4(c)).

The presence of wrinkles in the support layer, particularly at lower casting speeds, may be attributed to localized differential shrinkage during drying. The persistence of long cracks in some cases, despite variations in casting speed, suggests that internal stress distribution during drying is a critical factor that is not entirely mitigated by adjusting speed alone.

Nevertheless, both tapes, irrespective of the presence of long cracks, are found to be suitable for producing disks with diameters ranging from 110 mm to 20 mm, as illustrated in Fig. 4(d), owing to their preserved long-range structural integrity and uniformity.

3.3.2. *Thermal processing: debinding, sintering and flattening*

Bilayer tapes, as represented by the obtained green ceramic disks, are investigated for compatibility between the membrane and support layers during thermal processing. These bilayer structures were fabricated through sequential tape casting, where distinct blade gaps were employed to control layer thickness. The ceramic slurries used for each layer were prepared using powders of varying particle sizes to optimize packing density, porosity, and mechanical integration between the layers.

(1) Bilayer tape from blade gaps of 0.1 mm for the membrane and 1 mm for the support

The sintering behavior of the bilayer tape I is reflected through the shrinkage dynamics observed during thermal treatment. This was captured by tracking the side-view profile evolution of a 30 mm-diameter green disk, with the membrane layer positioned on top, using an optical dilatometer [35]. Thermal treatment was carried out at a uniform heating and cooling rate of 5 K/min, and the results are graphically presented in Fig. 5(a). The series of optical images represent the disk profiles at the conclusion of distinct thermal steps. To elucidate these phenomena further, the shrinkage behavior of each individual layer is schematically illustrated in Fig. 5(b), which demonstrates a stepwise evolution as described below:

- Step 0: during heating up to 900 °C, the disk exhibits slight warping towards the support side. This is primarily attributed to a greater volumetric contraction in the support layer, driven by the combustion of the corn starch present within the support tape;
- Step 1: between 900 °C and 1350 °C, the disk progressively flattens. This suggests that the membrane layer initiates its sintering process slightly earlier than the support layer, resulting in marginally greater shrinkage at this stage;
- Step 2: while dwelling at 1350 °C for a duration of 2 h and 24 min, the disk gradually warps towards the membrane side. This reflects a markedly accelerated sintering process in the membrane layer relative to the support;
- Step 3: continuing the dwell at 1350 °C from 2 h and 24 min to 4 h and 57 min, the disk once again flattens. This indicates that the shrinkage rate of the membrane layer has slowed down, while the shrinkage of the support layer has accelerated;
- Step 4: between 4 h and 58 min and 6 h (~1 h in total) at 1350 °C, no significant morphological changes are observed. This points to a period of synergistic sintering, wherein the rates of shrinkage for both layers become comparable;
- Step 5: during the final phase of dwelling, from 6 h to 10 h, the disk begins to warp towards the support side. At this point, the shrinkage of the membrane layer is practically complete, while the support layer continues to undergo shrinkage.

This comprehensive analysis of the shrinkage dynamics highlights a critical time window, specifically in Step 4, during which flat, asymmetric membranes can be optimally produced. Based on this insight, a sintering profile of 1350 °C for a duration of 5 h was employed to sinter multiple disks. As shown in Fig. 5(c), optical images of the sintered disks reveal that those with initial diameters of 20 mm and 30 mm exhibit near-flat surfaces, free from visible cracking on the membrane side. However, the disk with an initial 40 mm diameter shows significant membrane layer cracking, attributable to the larger relative shrinkage mismatch between the membrane and support layers.

Despite the successful formation of flat and crack-free disks, none achieved gas-tightness, suggesting that the membrane layers did not fully densify during the sintering process. Even after extending the dwelling time to 10 h, the disks remained gas-permeable, in contrast to the individual membrane layer disks (as analysed in section 3.2), which exhibited full gas-tightness under identical sintering conditions. This discrepancy highlights that the densification behavior of the membrane layer is profoundly affected by the presence of the support layer. A key mechanism likely contributes to this effect:

During thermal treatment at 1350 °C, particularly during stages of differential shrinkage between the layers (corresponding to Steps 2, 3, and 5), the membrane experiences mechanical constraints imposed by the support layer, which limits its ability to reach full densification.

Prolonging the dwelling time beyond 10 h at 1350 °C was deliberately circumvented due to the increased likelihood of pronounced warping, heightened risk of cracking, and undesirable densification of the support structure. Instead, a secondary thermal treatment was conducted at a reduced temperature of 1300 °C over an extended period of 15 h. This modified protocol successfully yielded crack-free and gas-tight disks (with initial diameters of 20 mm), though warping was observed (not shown here).

(2) Bilayer tape from blade gaps of 0.2 mm for the membrane and 0.75 mm for the support

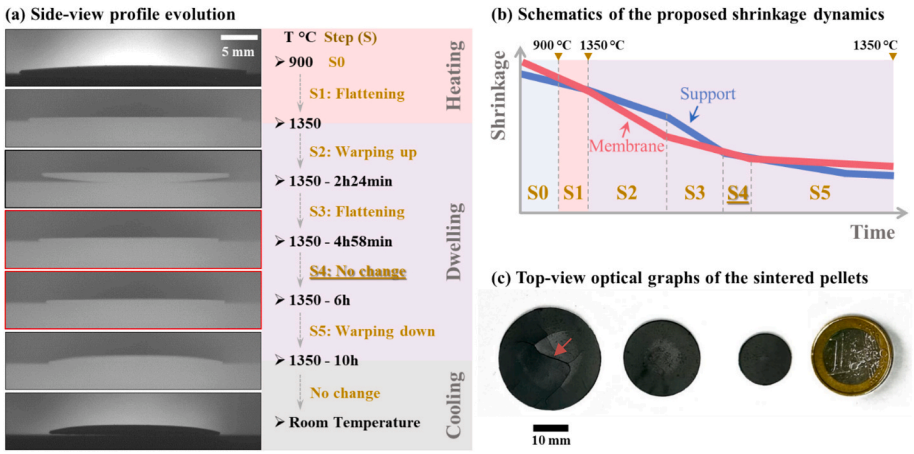

Fig. 5. Shrinkage dynamics of green disks (30 mm diameter) from bilayer tape I: (a) side-view profile evolution with the membrane layer on top during thermal treatment at a heating and cooling rate of 5 K/min, and (b) conceptual schematics illustrating the proposed shrinkage dynamics of each individual layer. In (c), optical graphs (top view of the membrane surface) of disks subjected to sintering at 1350 °C for 5 h are presented. The initial diameters of the disks, from left to right, measure 40 mm, 30 mm, and 20 mm, respectively. In (c), the cracks are indicated by the arrows. (For interpretation of the references to color in this figure legend, the reader is referred to the web version of this article.)

To alleviate the influence of the support layer on the membrane's densification, the blade gaps for the support layer was strategically reduced to 0.75 mm, while the one for the membrane layer was increased to 0.2 mm. This modification aimed to increase the thickness ratios between membrane and support layers from 0.1 to ~0.27, thereby reducing the layer thickness difference and improving structural integrity during sintering. The sintering behavior of the fabricated bilayer tape IV was further evaluated using disk specimens with initial diameters of 30 mm and 40 mm, as illustrated in Fig. S4. Both disks exhibited analogous thermally induced changes, as elaborated in Section 3.3.2*(1)*. Notably, when compared to the 30 mm disks derived from bilayer tape I (Fig. 5a), the most prominent deviation pertains to the duration of stage S4. Specifically, this stage was substantially shortened in bilayer tape IV specimens, with the time window for S4 reduced to approximately 41 min for the 30 mm disk and further contracted to around 15 min for the 40 mm disk. These variations confirm that while absolute sintering profiles differ across systems, the underlying shrinkage behavior and methodology for profile optimization remain robust.

The green disks from bilayer tape II, with an initial diameter of 20 mm, exhibited promising results. After sintering at 1350 °C for 4 h, the disks remained crack-free and gas-tight. Notably, the flatness of the disks was influenced by the type of ceramic powders: only the disks from bilayer tape II (prepared from as-received powders) maintained near-perfect flatness, while the ones from bilayer tapes III, IV and VI (prepared from ball-milled powders) are still warped.

However, for larger disks with initial diameters exceeding 30 mm, the same sintering conditions led to increased incidences of warping and cracking across all kinds of bilayer tapes. A clear example of this failure mode is shown in Fig. 6(a), where a sintered disk, initially 65 mm in diameter, contains a long crack, nearly bisecting the entire structure. The region surrounding the crack displayed substantial warping, suggesting that sintering continued well after the crack formation. This observation points to an early-stage initiation of cracking, likely during the debinding process up to 900 °C (corresponding to Step 0 in section 3.3.2*(1)*). During this stage, the support layer undergoes a more pronounced volumetric reduction compared to the membrane layer, leading to mechanical stresses that can easily fracture the loosely packed and non-sintered membrane layer.

To address this issue, an effective strategy was employed by slowing down the debinding process between 200 °C and 900 °C. A reduced heating rate of 0.5 K/min allows the unsintered and ductile ceramic tapes to deform gradually and uniformly, compensating for the shrinkage mismatch between the layers without inducing failure. This

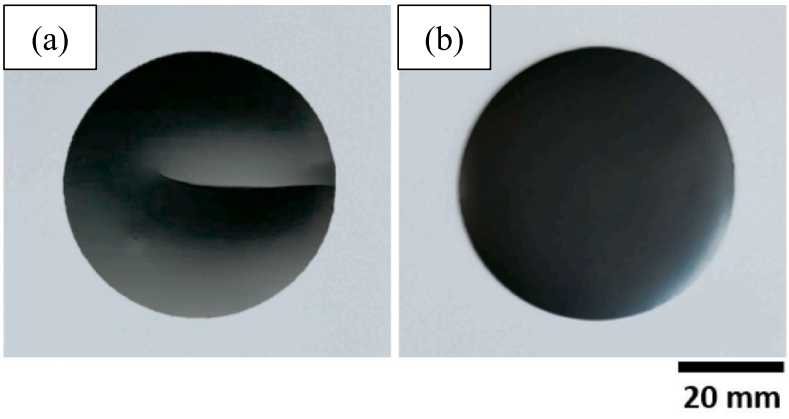

Fig. 6. Optical graphs (top view of the membrane surface) of disks sintered at 1350 °C for 4 h, under two distinct thermal profiles: (a) a uniform heating/cooling rate of 5 K/min across the entire temperature range, and (b) a reduced heating rate of 0.5 K/min applied exclusively between 200 °C and 900 °C. Both disks, initially 65 mm in diameter, were punched from bilayer tapes as shown in Fig. 4(b).

adjustment significantly improved the structural stability, as demonstrated in Fig. 6(b), as all disks, as large as ca. 50 mm in diameter, were crack-free after sintering. Approximately 60 % of the disks achieved gas-tightness after 4 h of sintering. Extending the dwell time to 8 h results in nearly all disks reaching gas-tightness, underscoring the importance of controlled thermal management during debinding and sintering for larger bilayer ceramic structures.

The optimized sintering program has facilitated an impressive upscaling of crack-free disks to a diameter of approximately 87 mm after sintering. Further upscaling is likely possible, but is not yet performed. Despite this success, the challenge of warpage remains, with its conditions evidently influenced by both the ceramic powders utilized and the dimensions of the samples. For instance, as illustrated in Fig. 7(a–c), the profiles of samples, initially 65 mm in diameter, show distinct warping depending on the ceramic powders used. When as-received ceramic powders were used, sintering at 1350 °C for 4 h induces an upward, uneven warping at the edges, particularly toward the membrane side. Conversely, samples made from ball-milled powders warp downward, i.e., toward the support side. The most uniform warping was observed in the sample made from ceramic powder ball-milled for one day, as demonstrated in Fig. 7(b), suggesting that the more uniform particle packing and green density promotes homogenous shrinkage during sintering.

However, the uniformity of warpage decreases as the sample diameter increases, as highlighted in Fig. 7(d) and (e). This reduction correlates with the decreased structural uniformity as the surface area increases, which leads to less consistent shrinkage across the sample.

To address warping, homogeneously warped samples were selected for flattening, which offers better load distribution and stabilization points. Initial flattening attempts at 1200 °C under a pressure of approximately 0.2 g/mm^2 were unsuccessful, even after 10 h, as shown in Fig. 7(f). Increasing the temperature to 1300 °C markedly improved results, as a lower load of 0.1 g/mm^2 and a shorter hold time of 1 h significantly reduced warpage (Fig. 7(g)). Further extending the hold time to 4 h produced an almost fully flattened sample, with minor edge curvatures remaining (Fig. 7(h)). These edge imperfections were then mitigated by increasing the load to 0.2 g/mm^2, resulting in a nearly flat sample, as shown in Fig. 7(i).

This analysis suggests that optimizing both the powder treatment and sintering conditions can significantly enhance the dimensional stability of large ceramic samples, with warpage being manageable through precise control of temperature, load, and holding time. Table 2 presents a consolidated overview of the optimized processing parameters and material configurations that governed the successful upscaling of asymmetric membrane fabrication.

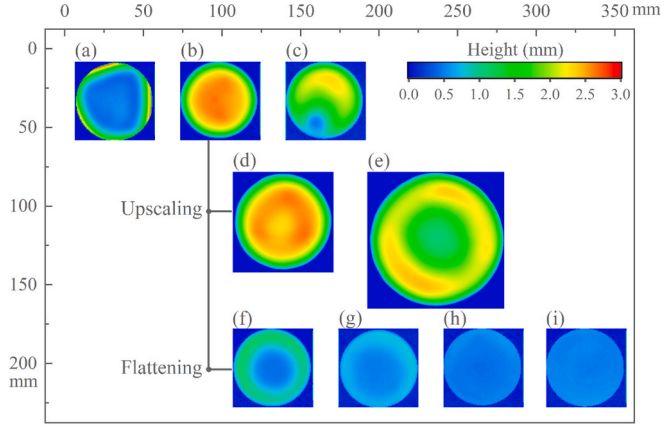

Fig. 7. Topographies of membrane surfaces for both as-sintered (a–e) and post-flattened (f–i) asymmetric membranes. The membranes were fabricated from bilayer tape II (a), IV (b, d, e), and VI (c). The sintering was performed at 1350 °C for 4 h. Post-sintering flattening processes were applied to samples with profiles similar to (b). These samples underwent thermal treatment at 1200 °C for 10 h under a nominal pressure of 0.2 g/mm^2 (f), and at 1300 °C with different conditions: 1 h under 0.2 g/mm^2 (g), 4 h under 0.1 g/mm^2 (h), and 4 h under 0.2 g/mm^2 (i). The nominal pressure is calculated via normalizing the total load by the entire membrane area.

3.4. Membrane characterization

3.4.1. Crystal structure and microstructure

The XRD analysis of the as-received powders, as provided in Fig. 8(a), reveals peak splitting across all individual 2θ positions, both of which can be indexed to cubic ABO_3 perovskite structures. This peak splitting is indicative of compositional inhomogeneity, likely arising from the minor strontium deficiency. Rietveld refinement (refer to Fig. S5(a)) further identifies the coexistence of two distinct perovskite phases in the as-received powders: the dominant phase exhibits a lattice parameter of 3.907 Å, comprising approximately 79 wt%, while the other one, with a slightly smaller lattice parameter of 3.891 Å, constitutes roughly 21 wt%. Given that the unit cell volume of $SrTiO_3$ contracts with increased Fe substitution at the Ti site [11], the phase with the larger lattice constant is likely Fe-lean, whereas the smaller lattice phase corresponds to an Fe-rich composition.

The persistence of peak splitting following sintering under all examined conditions (Fig. 8(b–e)) confirms the retention of these dual perovskite phases throughout the sintering process, as exemplified by the inset in Fig. 8(e). Nonetheless, secondary phases begin to emerge with prolonged sintering times and higher sintering temperatures. Specifically, certain secondary reflections, absent in the sample sintered at 1350 °C for 4 h (Fig. 8(b)), become more pronounced after 10 h of sintering at the same temperature, as observed in Fig. 8(c). This trend is further accentuated in the sample sintered at 1400 °C for 10 h, where intense non-perovskite peaks appear at several 2θ positions (Fig. 8(d)). According to Rietveld refinement (Fig. S5(b)), these peaks correspond to a textured $SrFe_{12}O_{19}$ phase, comprising approximately 15 wt%. However, the $SrFe_{12}O_{19}$ phase almost disappears within the bulk of the sample, as demonstrated in Fig. 8(e). Rietveld refinement (Fig. S5(c)) confirms compositional evolution of the perovskite phases: after sintering at 1400 °C for 10 h, the Fe-lean perovskite phase slightly decreases in content (~68 wt%) while its lattice parameter increases to 3.913 Å. Simultaneously, the Fe-rich perovskite increases to ~32 wt% and its lattice parameter slightly increases to 3.905 Å.

To further elucidate the variation in Fe concentration within the perovskite phase, elemental mapping was performed via EDS on a polished cross-section of the specimen sintered at 1350 °C for 4 h. The corresponding elemental distribution maps are presented in Fig. 8(f–i). The data distinctly reveal a heterogeneous distribution of Fe and Ti

Table 2
Optimized processing parameters and material configurations enabling successful upscaling of asymmetric membrane fabrication.

Step	Parameter	Value/Selection
Tape casting	Pore former for the support	Corn starch
	Powder average particle size	0.8 μm
	Powder specific surface area	4.6 m^2/g
	Blade heights	Support: 0.75 mm
		Membrane: 0.20 mm
	Casting speed	2.5 mm/s
Sintering§	Temperature	1350 °C
	Heating rate from 200 °C–900 °C	0.5 K/min
	Holding time	4 h
Flattening§	Load	0.2 g/mm^2
	Temperature	1300 °C
	Holding time	4 h

§: the heating and cooling rates were set at 5 K/min unless specified.

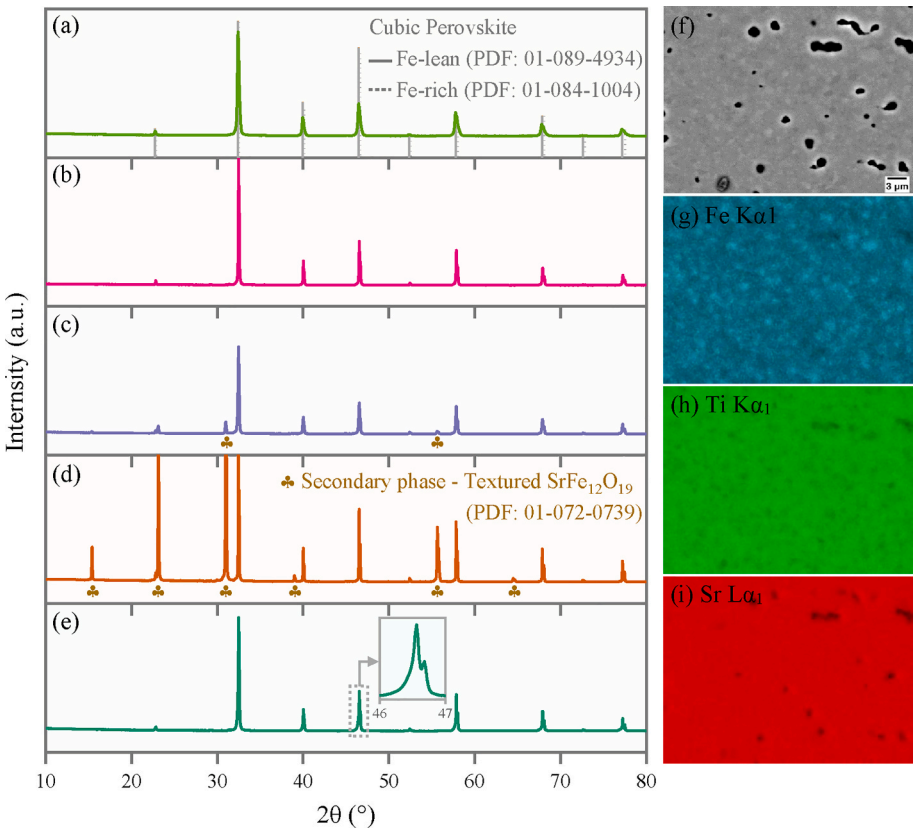

Fig. 8. Phase composition analyzed by XRD (a–e) and EDS (f–i). XRD patterns are presented for (a) the as-received powders, and (b–e) samples sintered at varied thermal profiles: (b) 1350 °C for 4 h, (c) 1350 °C for 10 h, and (d, e) 1400 °C for 10 h. (b–d) are analyzed at the as-sintered surfaces, while (e) represents the deeply polished surface. Elemental mapping (f–i) was conducted on the polished cross-section of the sample sintered at 1350 °C for 4 h, with the associated BSEM micrograph shown in (f).

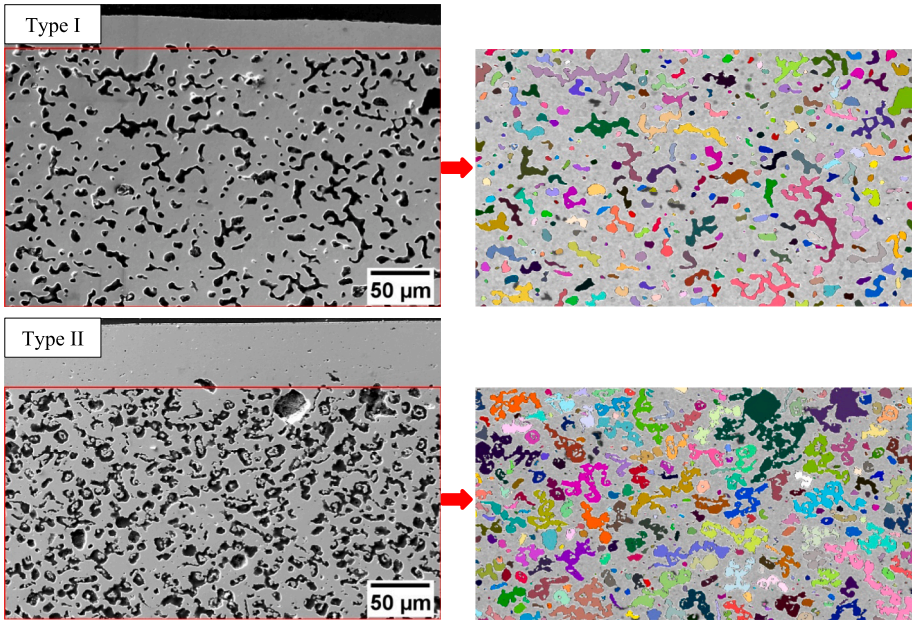

Fig. 9. Cross-sectional SEM microstructures (left column) of type I and II asymmetric membranes with two distinct layer configurations prepared and sintered from bilayer tape I and II, respectively. Pores/pore agglomerates in the red-framed support layers are segmented and color-coded (right column) based on BSEM contrast. For Type I, the sintering was performed firstly at 1350 °C for 10 h and then at 1300 °C for 15 h. While for Type II, the sintering was finalized after annealing at 1350 °C for 4 h. (For interpretation of the references to color in this figure legend, the reader is referred to the web version of this article.)

across the microstructure, in contrast to the relatively uniform distribution of Sr (excluding pore regions, which appear as black due to signal absence). Notably, Fe-enriched grains coincide with Ti-depleted regions, suggesting significant local variation in the Fe:Ti ratio among individual grains. This compositional disparity is closely correlated with the peak splitting observed in the XRD patterns, indicative of compositional heterogeneity within the perovskite phase. However, due to the current resolution limitations, precise quantification of these elemental ratios remains challenging. Further high-resolution and quantitative analytical techniques will be required to validate the exact composition.

The microstructures of two types of gas-tight asymmetric membranes are compared in Fig. 9. They are processed from bilayer tape I and II. These two tapes were obtained via using different blade gaps as provide in Table 1. The sintered programs are also differed as mentioned in the previous sections and detailed in the following:

- Type I asymmetric membrane was obtained from bilayer tape I. The sintering procedure was conducted in two stages, including an initial stage at 1350 °C for 10 h, followed by a secondary stage at 1300 °C for 15 h.
- Type II asymmetric membrane was obtained from bilayer tape II, with sintering completed in a single annealing step at 1350 °C for 4 h.

These variations in blade gaps and sintering programs, result in distinguishable structural characteristics between the two membranes, particularly concerning layer thicknesses and porosities. The total thickness of both membranes remains comparable, while the individual layer thicknesses vary (see Table 3): the membrane layer thickness in Type II is approximately double that of Type I, balanced by a corresponding reduction in the support layer thickness. The increased blade gap in the Type II casting process is associated with a thicker membrane layer.

Porosity also differs significantly between the two membranes. Although membrane layer porosities are negligible in both structures, the support layers exhibit marked differences. As illustrated in Fig. 9, all pores in the support layers were segmented, with connected or agglomerated pores identified by a shared color code. The support layer in Type II displays a porosity of ~42 % (Table 3), nearly double that of Type I. Furthermore, the support layer in Type II demonstrates extensive pore agglomeration, indicative of enhanced pore connectivity. This increase in porosity and pore connectivity for Type II correlates with the shorter annealing duration, which limits sintering of the support structure. Such an open porous structure provides gas permeability essential for membrane function, while reduces the mechanical strength [17,44]. A particularly large elliptical defect, with a maximum diameter of ~89 μm, was detected approximately 63 μm beneath the surface of the Type II membrane layer, as shown in Fig. S6. When the membrane layer surface is under tensile due to a tensile or flexural load, this near-surface defect may act as fracture origin [45]. Based on the defect size and location, the corresponding mechanical strength was estimated to range between ~36 and 80 MPa, as derived from the fracture mechanics analysis detailed in Supplementary Note 1. These findings necessitate future efforts to minimize large defects within the support layer to enhance the structural reliability of the membrane.

Table 3
Structural characteristics of the two asymmetric membranes as shown in Fig. 9.

Membrane	Thickness (μm)		Porosity (%)	
	Membrane	Support	Membrane	Support
Type I	25 ± 6	360 ± 13	<1	22 ± 2
Type II	51 ± 1	331 ± 13	<1	42 ± 3

3.4.2. Oxygen permeation

(1) Bare single-layer membranes

For bare single-layer membranes, oxygen permeance is closely influenced by factors like temperature, thickness, and the presence of surface secondary phases. According to the Wagner model, oxygen permeance decreases with a reduction in operational temperature, while increase with decreasing of thickness, as observed in Fig. 10 (a) and (b), respectively.

For the thinnest membranes evaluated in this study, variations in surface secondary phases notably impact performance. Two of these samples were densified at 1400 °C and 1350 °C for 10 h, respectively, exhibiting comparable permeances, despite differing amounts of surface secondary phases, as revealed by Fig. 8. Further investigation reveals that surface polishing, a process employed to remove secondary phases, markedly increases permeance. This result unveils the role of secondary phases as barriers to surface exchange kinetics, thereby reducing effective oxygen permeance. Secondary phases may act as local points of resistance, decreasing surface reactivity and impeding the exchange of oxygen ions at the membrane interface.

To mitigate the detrimental effects of surface secondary phases, membranes sintered at 1400 °C for 10 h were polished to varying thicknesses for measuring and comparing oxygen permeance. The permeance values, as plotted in Fig. 10(b), were fitted using Eq. (5) under the assumption that $L + L_c \approx L$, i.e., neglecting the contribution of surface exchange. The data points, excluding those corresponding to the thinnest membrane (approximately 223 μm), align well with the linearly fitted curves, suggesting a negligible surface exchange effect.

For the thinnest membrane, however, slight deviations between the measured and linearly fitted oxygen permeance values indicate a certain contribution from surface exchange. Nevertheless, this effect remains limited in magnitude. To achieve a more comprehensive characterization of surface exchange phenomena, additional data sets at reduced membrane thicknesses are required. This will be addressed by incorporating data from asymmetric membranes, and discussed in subsequent sections.

(2) Bare asymmetric membranes

Asymmetric membranes can present distinct oxygen permeance characteristics when compared to single-layer membranes, primarily due to the additional porous support layers. These support layers reduce the diffusibility of feed gas and introduces an oxygen concentration gradient from the external surface of the support layer to the support/membrane interface [15,20], thereby reducing the driving force for oxygen permeation. Consequently, oxygen permeance values determined without accounting for gas diffusion resistance may be underestimated.

Given the high porosity of the support layer (see Table 3), the Type II asymmetric membrane is expected to experience minimal gas diffusion resistance, allowing it to function similarly to a single-layer membrane. Accordingly, the oxygen permeance data for the Type II asymmetric membrane were modeled alongside those of polished single-layer membranes, following the methodology outlined in Section 2.2.5. The unpolished surface for the Type II asymmetric membrane is unlikely to exert a significant influence, as the applied sintering profile does not result in noticeable secondary phase formation, as discussed in Section 3.4.1. This modeling approach enables the precise extraction of key transport parameters, including characteristic thickness and ambipolar conductivity (Table 4), which facilitate more accurate performance predictions for membranes of varying thicknesses. The ambipolar conductivity exhibits a slight decline with decreasing temperature, consistent with the semiconducting behavior inferred from the combined ionic and electronic transport mechanisms. Theoretically, the characteristic thickness is expected to exhibit a parallel temperature dependence.

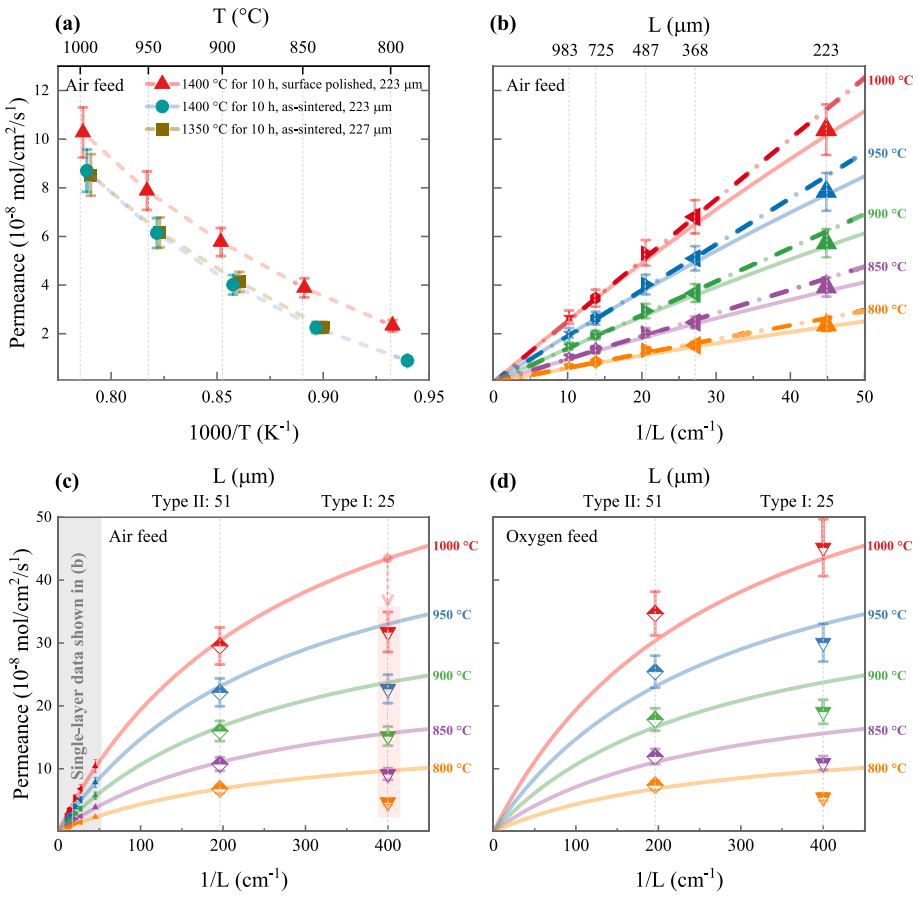

Fig. 10. Oxygen permeance of surface-polished single-layer membranes as a function of temperature (a) and membrane thickness (b) when air was used as the feed gas, along with the oxygen permeance of asymmetric membranes when exposed to air (c) and pure oxygen (d) as the feed gas. In (b), the dash-dotted lines represent the linear fits derived from the oxygen permeance of single-layer membranes under the assumption that surface exchange effects are negligible. In contrast, the solid lines in (b), (c) and (d) correspond to parameter fitting results that incorporate surface exchange effects, based on the oxygen permeance data from both single-layer (surface-polished) and Type II asymmetric membranes.

Table 4
Ambipolar conductivities and characteristic thicknesses obtained from parameter fitting based on oxygen permeances of single-layer (surface-polished) and Type II asymmetric membranes.

Temperature (°C)	Ambipolar conductivity (S/m)	Characteristic thickness (μm)
1000	3.69	17.7
950	2.92	17.7
900	2.21	18.0
850	1.56	18.8
800	0.99	18.1

However, this trend is not clearly captured by the current data fitting, as presented in Table 4. A plausible explanation for this discrepancy is the relatively limited variation in the characteristic thickness, which likely falls within the range of experimental uncertainties that are difficult to quantify with precision under the present measurement conditions.

Utilizing these modeled parameters, the corresponding solid lines are plotted in Fig. 10(b, c, d). The close alignment between the measured oxygen permeance values under air feeding and those obtained from parameter fitting reinforces the reliability of the overall assumptions and interpretations.

In contrast, the permeances of the Type I asymmetric membrane is notably lower than the values on the fitted curves and falls below the permeance of the Type II membrane (see Fig. 10(c)), despite its thinner membrane layer. This indicates significant permeance underestimation, and is closely associate to the lower porosity within the Type I support layer (see Table 3), which contributes to greater resistance against oxygen binary gas diffusion, resulting in a dominant negative effect from the support layer.

Upon switching the feed gas from air to pure oxygen, both Type I and Type II asymmetric membranes exhibit notable permeance increases, particularly at high temperatures, as illustrated in Fig. 10(d). The introduction of pure oxygen as the feed gas: (i) increase the driving force, (ii) reduces or even eliminates the partial pressure drop across the support layer, and (iii) enhances surface exchange kinetics – both of which promote oxygen permeation. The latter effect is likely the dominant factor driving the permeance increase above 900 °C for Type II asymmetric membranes. However, for Type I asymmetric membranes, it remains unclear which mechanism plays the dominating role.

Overall, these findings suggest that the Type II asymmetric structure is functionally superior to the Type I structure under comparable operational conditions.

(3) Coated asymmetric membranes

Applying surface coatings to membranes introduces additional active sites for oxygen exchange, particularly enhancing performance at lower temperatures, where surface exchange is sluggish.

A comparative analysis of the as-sintered and dip-coated membrane surfaces, as presented in Fig. 11, reveals pronounced morphological transformations induced by the coating process. Two distinct porous layers were successfully deposited via dip-coating. Among them, the LSCF layer demonstrates a more uniform and extensive surface coverage

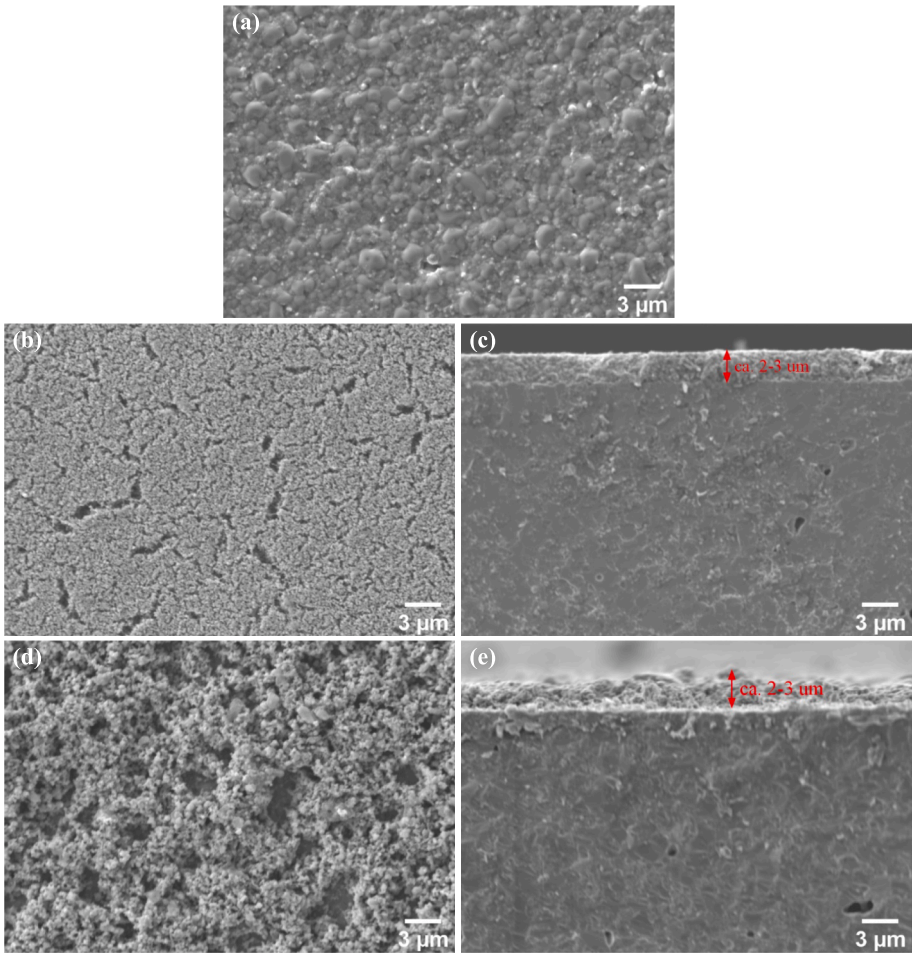

Fig. 11. Microstructures of membranes: (a) uncoated membrane (top surface view); (b, c) membrane coated with LSCF: (b) top surface view, (c) cross-sectional view; (d, e) membrane coated with S98TF25: (d) top surface view, (e) cross-sectional view.

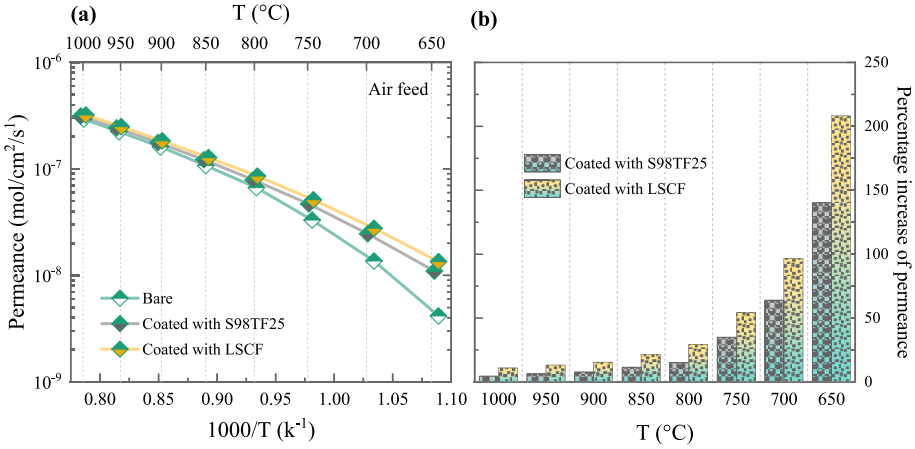

Fig. 12. Oxygen permeances (a) and the corresponding percentage increase (b) measured for coated Type II asymmetric membranes as compared with the bare one. Air was applied as the feed gas for the measurements. An inset micrograph in (b) provides an example of the LSCF coating morphology.

relative to the S98TF25 layer, although both coatings exhibit comparable thicknesses in the range of approximately 2–3 μm. These observations underscore the influence of coating composition and initial powder characteristics, e.g., particle size, on film uniformity and microstructural integration with the underlying membrane substrate.

Experimental data (Fig. 12) indicate that coating effects are minimal within the high-temperature range (1000 °C–800 °C), but becomes significant at lower temperatures (750 °C–650 °C), as shown by the substantial increases in permeance (Fig. 12(b)) and reduced activation energies (see Table 5).

Between the two coatings, LSCF demonstrates superior performance, yielding higher permeance values and lower activation energies than S98TF25. This enhanced behavior can be attributed to a combination of intrinsic material properties and morphological differences. Specifically,

Table 5
Activation energies of oxygen permeances of bare and coated Type II asymmetric membranes.

Surface coating	Activation energy (kJ/mol)	
	1000 °C–850 °C	750 °C–650 °C
None	76 ± 1	160 ± 11
S98TF25	72 ± 1	113 ± 3
LSCF	71 ± 1	104 ± 3

LSCF has a superior mixed conductivity and faster surface exchange kinetics than S98TF25 [46], facilitating more efficient surface activation. Additionally, the LSCF coating exhibits a more uniform and continuous morphology, further supporting their improved performance. However, it should be noted that LSCF is chemically unstable under reducing conditions, e.g., syngas at high temperatures, which limits its applicability.

The pronounced effectiveness of these coatings at low temperatures highlights the importance of surface modifications in optimizing oxygen permeance for asymmetric membranes.

4. Conclusions

This research delivers a comprehensive exploration of successive tape casting as a scalable method for producing high-performance, planar asymmetric oxygen transport ceramic membranes. We have methodically adjusted key manufacturing parameters, starting with commercially sourced ceramic powders, to create bilayer membranes with enhanced structural compatibility, mechanical integrity, and functional performance.

Maintaining the mechanical stability of ceramic tapes requires precise control of powder particle size through optimized ball milling. By keeping specific surface areas below 5 m^2/g and average particle sizes above 0.6 μm, a balance was struck that improved homogeneity in green densities and prevented cracking.

The compatibilities of the bilayer membranes are demonstrated to be depend critically on the choice of pore former, as well as specific tape casting and sintering parameters. In particular, the incorporation of corn starch as a pore former proved instrumental in minimizing shrinkage discrepancies across layers, promoting dimensional stability. The bilayer tapes, cast using blade gaps of 0.75 mm for the support layer and 0.2 mm for the membrane layer, enabled a successful one-step sintering process at 1350 °C, yielding the desired asymmetric membrane structure. Preventing cracks in large-sized membranes with diameters up to ~87 mm was made possible by utilizing a cautious heating rate of 0.5 K/min between 200 °C and 900 °C during debinding procedure. Furthermore, the sample warpages are effective overcome by post-annealing at 1300 °C for 4 h at a nominal load of 0.2 g/mm^2.

In functional characterization, this study provides thorough evaluations of oxygen permeation performance with considerations on phase and microstructural characteristics. The surface secondary phases were evident to be detrimental, which were eliminated by shorter sintering durations (4 h at 1350 °C), negating the necessity for surface polishing. A highly porous support layer with a wide surface area and rapid gas diffusion pathways was also produced by this optimized sintering profile, which contributed to improved oxygen permeation performance. Additional performance gains were obtained by using microsized porous coatings, with LSCF coatings proving particularly advantageous at lower operational temperatures (650 °C to 750 °C) due to superior intrinsic surface exchange kinetics compared to S98TF25.

This work exemplifies the integration of manufacturing control and functional evaluation to pave the way for next-generation oxygen transport membranes. These developments offer practical solutions for improving scalability and efficiency in industrial applications, ranging from oxygen production and energy conversion to chemical synthesis, positioning these membranes as valuable components in sustainable industrial technologies.

CRediT authorship contribution statement

Fanlin Zeng: Writing – original draft, Visualization, Software, Resources, Methodology, Investigation, Formal analysis, Data curation, Conceptualization. **Wendelin Deibert:** Writing – review & editing, Validation, Supervision, Software, Resources, Methodology, Investigation, Conceptualization. **Kai Wilkner:** Writing – review & editing, Validation, Software, Methodology, Investigation, Formal analysis, Data curation. **Wilhelm Albert Meulenberg:** Writing – review & editing, Validation, Supervision, Resources, Project administration, Funding acquisition. **Stefan Baumann:** Writing – review & editing, Validation, Supervision, Software, Resources, Project administration, Methodology, Investigation, Funding acquisition, Formal analysis, Data curation, Conceptualization.

Declaration of competing interest

The authors declare that they have no known competing financial interests or personal relationships that could have appeared to influence the work reported in this paper.

Acknowledgements

The work is funded by Federal Ministry of Education and Research (BMBF, Germany) – 03SF0648A. The authors acknowledge Dr. Y. J. Sohn for XRD analysis, Mr. S. Heinz for permeation testing, and Mr. J.-P. Nacke for powder and slurry preparation as well as Prof. Dr.-Ing. O. Guillon and Dr.-Ing. Nicole Carina Neumann for support.

Appendix A. Supplementary data

Supplementary data to this article can be found online at https://doi.org/10.1016/j.seppur.2025.134064.

Data availability

Data will be made available on request.

References

[1] X. Zhu, W. Yang, Mixed Conducting Ceramic Membranes, Springer-Verlag, Berlin, Germany, 2017.
[2] L.L. Anderson, P.A. Armstrong, R.R. Broekhuis, M.F. Carolan, J. Chen, M. D. Hutcheon, C.A. Lewinsohn, C.F. Miller, J.M. Repasky, D.M. Taylor, Advances in ion transport membrane technology for oxygen and syngas production, Solid State Ion. 288 (2016) 331–337.
[3] M. Czyperek, P. Zapp, H.J.M. Bouwmeester, M. Modigell, K. Ebert, I. Voigt, W. A. Meulenberg, L. Singheiser, D. Stöver, Gas separation membranes for zero-emission fossil power plants: MEM-BRAIN, J. Membr. Sci. 359 (2010) 149–159, https://doi.org/10.1016/j.memsci.2010.04.012.
[4] C. Descamps, C. Bouallou, M. Kanniche, Efficiency of an Integrated Gasification Combined Cycle (IGCC) power plant including CO_2 removal, Energy 33 (2008) 874–881, https://doi.org/10.1016/j.energy.2007.07.013.
[5] Y. Zhang, K. Su, F. Zeng, W. Ding, X. Lu, A novel tubular oxygen-permeable membrane reactor for partial oxidation of CH_4 in coke oven gas to syngas, Int. J. Hydrogen Energy 38 (2013) 8783–8789, https://doi.org/10.1016/j.ijhydene.2013.05.019.
[6] H. Jiang, H. Wang, S. Werth, T. Schiestel, J. Caro, Simultaneous production of hydrogen and synthesis gas by combining water splitting with partial oxidation of methane in a hollow-fiber membrane reactor, Angew. Chem. Int. Ed. 47 (2008) 9341–9344, https://doi.org/10.1002/anie.200803899.
[7] W. Fang, F. Steinbach, Z. Cao, X. Zhu, A. Feldhoff, A highly efficient sandwich-like symmetrical dual-phase oxygen-transporting membrane reactor for hydrogen production by water splitting, Angew. Chem. Int. Ed. 55 (2016) 8648–8651, https://doi.org/10.1002/anie.201603528.
[8] Z. Cao, H. Jiang, H. Luo, S. Baumann, W.A. Meulenberg, J. Assmann, L. Mleczko, Y. Liu, J. Caro, Natural gas to fuels and chemicals: improved methane aromatization in an oxygen-permeable membrane reactor, Angew. Chem. Int. Ed. 52 (2013) 13794–13797.

[9] L. Cai, Z. Cao, X. Zhu, W. Yang, Effects of catalysts on water decomposition and hydrogen oxidation reactions in oxygen transport membrane reactors, J. Membr. Sci. 634 (2021) 119394, https://doi.org/10.1016/j.memsci.2021.119394.

[10] G. He, W. Liang, C.-L. Tsai, X. Xia, S. Baumann, H. Jiang, W.A. Meulenberg, Chemical environment-induced mixed conductivity of titanate as a highly stable oxygen transport membrane, iScience, 19 (2019) 955-964. doi: 10.1016/j.isci.2019.08.032.

[11] F. Schulze-Küppers, S.F.P. ten Donkelaar, S. Baumann, P. Prigorodov, Y.J. Sohn, H. J.M. Bouwmeester, W.A. Meulenberg, O. Guillon, Structural and functional properties of $SrTi_{1-x}Fe_xO_{3-\delta}$ ($0\leqslant x\leqslant 1$) for the use as oxygen transport membrane, Sep. Purif. Technol. 147 (2015) 414–421, https://doi.org/10.1016/j.seppur.2014.12.020.

[12] A.A. Murashkina, E.Y. Pikalova, A.K. Demin, Promising membrane materials based on strontium titanate, Russ. J. Electrochem. 45 (2009) 542–547, https://doi.org/10.1134/S1023193509050073.

[13] A. Rothschild, W. Menesklou, H.L. Tuller, E. Ivers-Tiffée, Electronic structure, defect chemistry, and transport properties of $SrTi_{1-x}Fe_xO_{3-y}$ solid solutions, Chem. Mater. 18 (2006) 3651–3659, https://doi.org/10.1021/cm052803x.

[14] W. Menesklou, H.-J. Schreiner, K.H. Härdtl, E. Ivers-Tiffée, High temperature oxygen sensors based on doped $SrTiO_3$, Sens. Actuators B 59 (1999) 184–189, https://doi.org/10.1016/S0925-4005(99)00218-X.

[15] F. Schulze-Küppers, S. Baumann, W.A. Meulenberg, H.J.M. Bouwmeester, Influence of support layer resistance on oxygen fluxes through asymmetric membranes based on perovskite-type oxides $SrTi_{1-x}Fe_xO_{3-\delta}$, J. Membr. Sci. 596 (2020) 117704 https://doi.org/10.1016/j.memsci.2019.117704.

[16] S. Baumann, W.A. Meulenberg, H.P. Buchkremer, Manufacturing strategies for asymmetric ceramic membranes for efficient separation of oxygen from air, J. Eur. Ceram. Soc. 33 (2013) 1251–1261, https://doi.org/10.1016/j.jeurceramsoc.2012.12.005.

[17] A. Kaiser, S.P. Foghmoes, G. Pećanac, J. Malzbender, C. Chatzichristodoulou, J. A. Glasscock, D. Ramachandran, D.W. Ni, V. Esposito, M. Søgaard, P. V. Hendriksen, Design and optimization of porous ceramic supports for asymmetric ceria-based oxygen transport membranes, J. Membr. Sci. 513 (2016) 85–94, https://doi.org/10.1016/j.memsci.2016.04.016.

[18] S. Cheng, H. Huang, S. Ovtar, S.B. Simonsen, M. Chen, W. Zhang, M. Søgaard, A. Kaiser, P.V. Hendriksen, C. Chen, High-performance microchanneled asymmetric $Gd_{0.1}Ce_{0.9}O_{1.95-\delta}$-$La_{0.6}Sr_{0.4}FeO_{3-\delta}$-based membranes for oxygen separation, ACS Appl. Mater. Interf. 8 (2016) 4548–4560, https://doi.org/10.1021/acsami.5b10714.

[19] X. Shao, Z. Wang, S. Xu, K. Xie, X. Hu, D. Dong, G. Parkinson, C.-Z. Li, Microchannel structure of ceramic membranes for oxygen separation, J. Eur. Ceram. Soc. 36 (2016) 3193–3199, https://doi.org/10.1016/j.jeurceramsoc.2016.05.005.

[20] P.L. Rachadel, J. Motuzas, R.A.F. Machado, D. Hotza, J.C. Diniz da Costa, Influence of porous structures on O_2 flux of BSCF asymmetric membranes, Sep. Purif. Technol. 175 (2017) 164–169, https://doi.org/10.1016/j.seppur.2016.10.053.

[21] L. Chen, L. Liu, J. Xue, L. Zhuang, H. Wang, Asymmetric membrane structure: an efficient approach to enhance hydrogen separation performance, Sep. Purif. Technol. 207 (2018) 363–369, https://doi.org/10.1016/j.seppur.2018.06.066.

[22] Y. Wei, J. Xue, H. Wang, J. Caro, Hydrogen permeability and stability of $BaCe_{0.85}Tb_{0.05}Zr_{0.1}O_{3-\delta}$ asymmetric membranes, J. Membr. Sci. 488 (2015) 173–181, https://doi.org/10.1016/j.memsci.2015.04.035.

[23] Q. Li, X. Zhu, W. Yang, Single-step fabrication of asymmetric dual-phase composite membranes for oxygen separation, J. Membr. Sci. 325 (2008) 11–15, https://doi.org/10.1016/j.memsci.2008.08.002.

[24] X. Meng, W. Ding, R. Jin, H. Wang, Y. Gai, F. Ji, Y. Ge, D., Xie, Two-step fabrication of $BaCo_{0.7}Fe_{0.2}Nb_{0.1}O_{3-\delta}$ asymmetric oxygen permeable membrane by dip coating, J. Membr. Sci. 450 (2014) 291–298, https://doi.org/10.1016/j.memsci.2013.09.009.

[25] O. Büchler, J.M. Serra, W.A. Meulenberg, D. Sebold, H.P. Buchkremer, Preparation and properties of thin $La_{1-x}Sr_xCo_{1-y}Fe_yO_{3-\delta}$ perovskitic membranes supported on tailored ceramic substrates, Solid State Ion. 178 (2007) 91–99, https://doi.org/10.1016/j.ssi.2006.11.015.

[26] M.L. Fontaine, J.B. Smith, Y. Larring, R. Bredesen, On the preparation of asymmetric $CaTi_{0.9}Fe_{0.1}O_{3-\delta}$ membranes by tape-casting and co-sintering process, J. Membr. Sci. 326 (2009) 310–315, https://doi.org/10.1016/j.memsci.2008.10.009.

[27] G. Etchegoyen, T. Chartier, P. Del-Gallo, An architectural approach to the oxygen permeability of a $La_{0.6}Sr_{0.4}Fe_{0.9}Ga0.1O_{3-\delta}$ perovskite membrane, J. Eur. Ceram. Soc. 26 (2006) 2807–2815, https://doi.org/10.1016/j.jeurceramsoc.2005.06.025.

[28] S. Pirou, J. Gurauskis, V. Gil, M. Søgaard, P.V. Hendriksen, A. Kaiser, S. Ovtar, R. Kiebach, Oxygen permeation flux through 10Sc1YSZ-MnCo2O4 asymmetric membranes prepared by two-step sintering, Fuel Process. Technol. 152 (2016) 192–199, https://doi.org/10.1016/j.fuproc.2016.06.019.

[29] S. Pirou, J.M. Bermudez, B.T. Na, S. Ovtar, J.H. Yu, P.V. Hendriksen, A. Kaiser, T. R. Reina, M. Millan, R. Kiebach, Performance and stability of $(ZrO_2)_{0.89}(Y_2O_3)_{0.01}(Sc_2O_3)_{0.10}$-$LaCr_{0.85}Cu_{0.10}Ni_{0.05}O_{3-\delta}$ oxygen transport membranes under conditions relevant for oxy-fuel combustion, J. Membr. Sci. 552 (2018) 115–123.

[30] S. Baumann, J.M. Serra, M.P. Lobera, S. Escolástico, F. Schulze-Küppers, W. A. Meulenberg, Ultrahigh oxygen permeation flux through supported $Ba_{0.5}Sr_{0.5}Co_{0.8}Fe_{0.2}O_{3-\delta}$ membranes, J. Membr. Sci. 377 (2011) 198–205, https://doi.org/10.1016/j.memsci.2011.04.050.

[31] F. Schulze-Küppers, S. Baumann, F. Tietz, H.J.M. Bouwmeester, W.A. Meulenberg, Towards the fabrication of $La_{0.98-x}SrxCo_{0.2}Fe_{0.8}O_{3-\delta}$ perovskite-type oxygen transport membranes, J. Eur. Ceram. Soc. 34 (2014) 3741–3748, https://doi.org/10.1016/j.jeurceramsoc.2014.06.012.

[32] P. Fedeli, F. Drago, F. Schulze-Küppers, S. Baumann, Asymmetric LSCF membranes utilizing commercial powders, Materials (2020).

[33] F. Schulze-Küppers, F. Drago, L. Ferravante, S. Herzog, S. Baumann, P. Pinacci, W. A. Meulenberg, Design and fabrication of large-sized planar oxygen transport membrane components for direct integration in oxy-combustion processes, Sep. Purif. Technol. 220 (2019) 89–101, https://doi.org/10.1016/j.seppur.2019.03.052.

[34] W. Deibert, M.E. Ivanova, W.A. Meulenberg, R. Vaßen, O. Guillon, Preparation and sintering behaviour of $La_{5.4}WO_{12-\delta}$ asymmetric membranes with optimised microstructure for hydrogen separation, J. Membr. Sci. 492 (2015) 439–451, https://doi.org/10.1016/j.memsci.2015.05.065.

[35] W. Deibert, M.E. Ivanova, Y. Huang, R. Merkle, J. Maier, W.A. Meulenberg, Fabrication of multi-layered structures for proton conducting ceramic cells, J. Mater. Chem. A 10 (2022) 2362–2373, https://doi.org/10.1039/D1TA05240C.

[36] W. Deibert, M.E. Ivanova, K. Ran, J. Mayer, W.A. Meulenberg, Up-scaling and processing related characterisation of hydrogen permeation membranes based on pristine and Mo substituted $La_{28-x}W_{4+x}O_{54+1.5x}$, J. Eur. Ceram. Soc. 43 (2023) 121–129, https://doi.org/10.1016/j.jeurceramsoc.2022.09.033.

[37] M. Bäurer, H. Kungl, M.J. Hoffmann, Influence of Sr/Ti stoichiometry on the densification behavior of strontium titanate, J. Am. Ceram. Soc. 92 (2009) 601–606, https://doi.org/10.1111/j.1551-2916.2008.02920.x.

[38] C.A. Schneider, W.S. Rasband, K.W. Eliceiri, NIH image to ImageJ: 25 years of image analysis, Nat. Methods 9 (2012) 671–675, https://doi.org/10.1038/nmeth.2089.

[39] L.-K. Huang, M.-J.-J. Wang, Image thresholding by minimizing the measures of fuzziness, Pattern Recogn. 28 (1995) 41–51, https://doi.org/10.1016/0031-3203(94)E0043-K.

[40] J.H. Joo, G.S. Park, C.-Y. Yoo, J.H. Yu, Contribution of the surface exchange kinetics to the oxygen transport properties in $Gd_{0.1}Ce_{0.9}O_{2-\delta}$-$La_{0.6}Sr_{0.4}Co_{0.2}Fe_{0.8}O_{3-\delta}$ dual-phase membrane, Solid State Ion. 253 (2013) 64–69, https://doi.org/10.1016/j.ssi.2013.08.038.

[41] F. Zeng, J. Malzbender, S. Baumann, M. Krüger, L. Winnubst, O. Guillon, W. A. Meulenberg, Phase and microstructural characterizations for $Ce_{0.8}Gd_{0.2}O_{2-\delta}$-$FeCo_2O_4$ dual phase oxygen transport membranes, J. Eur. Ceram. Soc. 40 (2020) 5646–5652, https://doi.org/10.1016/j.jeurceramsoc.2020.06.035.

[42] P. Niehoff, S. Baumann, F. Schulze-Küppers, R.S. Bradley, I. Shapiro, W. A. Meulenberg, P.J. Withers, R. Vaßen, Oxygen transport through supported $Ba_{0.5}Sr_{0.5}Co_{0.8}Fe_{0.2}O_{3-\delta}$ membranes, Sep. Purif. Technol. 121 (2014) 60–67, https://doi.org/10.1016/j.seppur.2013.07.002.

[43] C. Li, W. Li, J.J. Chew, S. Liu, X. Zhu, J. Sunarso, Rate determining step in SDC-SSAF dual-phase oxygen permeation membrane, J. Membr. Sci. 573 (2019) 628–638, https://doi.org/10.1016/j.memsci.2018.12.044.

[44] Y. Zou, C. Gaudillere, J.E. Escribano, J.M. Serra, J. Malzbender, Microstructure, mechanical behavior and flow resistance of freeze-cast porous 3YSZ substrates for membrane applications, J. Eur. Ceram. Soc. 37 (2017) 3167–3176, https://doi.org/10.1016/j.jeurceramsoc.2017.03.056.

[45] ASTM C1322-15, in: Standard Practice for Fractography and Characterization of Fracture Origins in Advanced Ceramics, ASTM International, West Conshohocken, PA, 2015.

[46] W. Jung, H.L. Tuller, A new model describing solid oxide fuel cell cathode kinetics: model thin film $SrTi_{1-x}Fe_xO_{3-\delta}$ mixed conducting oxides-a case study, Adv. Energy Mater. 1 (2011) 1184–1191, https://doi.org/10.1002/aenm.201100164.